Two-dimensional nodal-loop half-metal in monolayer MnN

Shan-Shan Wang,[1,2] Zhi-Ming Yu,[2] Ying Liu,[2] Yalong Jiao,[2] Shan Guan,[3] Xian-Lei Sheng,[2,4,*] and Shengyuan A. Yang[2,5,†]

[1]*School of Physics, Southeast University, Nanjing 211189, China*

[2]*Research Laboratory for Quantum Materials, Singapore University of Technology and Design, Singapore 487372, Singapore*

[3]*State Key Laboratory of Superlattices and Microstructures, Institute of Semiconductors, Chinese Academy of Sciences, Beijing 100083, China*

[4]*Department of Physics, Key Laboratory of Micro-nano Measurement-Manipulation and Physics (Ministry of Education),
Beihang University, Beijing 100191, China*

[5]*Center for Quantum Transport and Thermal Energy Science, School of Physics and Technology,
Nanjing Normal University, Nanjing 210023, China*

Two-dimensional (2D) materials with nodal-loop band crossing have been attracting great research interest. However, it remains a challenge to find 2D nodal loops that are robust against spin-orbit coupling (SOC) and realized in magnetic states. Here, based on first-principles calculations and theoretical analysis, we predict that monolayer MnN is a 2D nodal-loop half-metal with fully spin-polarized nodal loops. We show that monolayer MnN has a ferromagnetic ground state with out-of-plane magnetization. Its band structure shows half metallicity with three low-energy bands belonging to the same spin channel. The crossing between these bands forms two concentric nodal loops centered around the Γ point near the Fermi level. Remarkably, the nodal loops and their spin polarization are robust under SOC due to the protection of a mirror symmetry. We construct an effective model to characterize the fully polarized emergent nodal-loop fermions. We also find that a uniaxial strain can induce a loop transformation from a localized single loop circling around Γ to a pair of extended loops penetrating the Brillouin zone.

I. INTRODUCTION

Two-dimensional (2D) materials have been attracting tremendous interest since the discovery of graphene [1–4]. Many remarkable physical properties of graphene are connect to its topological band structure, namely, the conduction and valence bands of graphene linearly cross at two isolated Fermi points in the Brillouin zone (BZ), which makes the low-energy electrons resemble 2D massless Dirac fermions [5]. With the rapid advance in experimental techniques, many new 2D materials have been fabricated in recent years [2–4] and, inspired by graphene, there is great interest to explore 2D materials with nontrivial band topology.

In 2D, topological band crossings can take the form of 0D nodal points and also 1D nodal loops. Several 2D nodal-loop materials have been proposed in theory [6–10], and nodal loops in monolayer Cu_2Si and monolayer CuSe have been confirmed in recent experiments [11,12]. Compared to nodal points, the condition for stabilizing nodal loops in 2D is typically more stringent.

Two factors related to electron spin play important roles in the stability of nodal loops. The first is the spin-orbit coupling (SOC). Without SOC, spin is a dummy degree of freedom (for nonmagnetic systems), which only introduces a trivial double degeneracy, and the electrons can be regarded as spinless fermions when analyzing the symmetry/topology protection.

However, when SOC is included, spin has to be explicitly considered. Particularly, the symmetry groups for electronic states need to be described by double-valued representations rather than single-valued ones. Because the number of double-valued representations for a group is generally less than their single-valued counterparts, a band crossing protected in the absence of SOC is usually destroyed when SOC is turned on. For example, the Dirac points in graphene and most other 2D materials are unstable under SOC [13]. To have a real Dirac point in 2D, a condition involving certain nonsymmorphic symmetries was proposed [14], and such spin-orbit Dirac point was recently found in the monolayer HfGeTe family and hourglass Weyl loops in monolayer GaTeI family materials [10,15]. Similarly, most nodal loops in 2D proposed so far are vulnerable against SOC. For example, the nodal loops in monolayer Cu_2Si and monolayer CuSe are protected by mirror symmetry in the absence of SOC, but they are removed when SOC is included [11,12]. Hence, to find a 2D material with nodal loop that is robust against SOC is a much more difficult task.

The second factor is the spin polarization associated with magnetic ordering. 2D magnetic materials with high spin polarization are much desired also from the application perspective because these materials are useful for compact spintronic devices. Nevertheless, magnetic orders break the time-reversal symmetry, which also makes the protection of nodal loops more challenging, especially in the presence of SOC. A few 2D magnetic nodal-loop materials have been reported, including Na_2CrBi trilayer [16], monolayer $CrAs_2$ [17], and single-layer $GdAg_2$ [18]. However, in these examples, both

*xlsheng@buaa.edu.cn
†shengyuan_yang@sutd.edu.sg

spin-up and spin-down states coexist near the Fermi level, which decreases the net spin polarization for the current carriers. It is thus most desirable to have nodal loops formed in a single spin channel around the Fermi level, i.e., to realize a nodal-loop half-metal state. In 3D, such a state was recently predicted for $Li_3(FeO_3)_2$ [19], which hosts two fully spin-polarized nodal loops. In 2D, such a nodal-loop half-metal has yet to be discovered.

In this work, based on first-principles calculations, we reveal monolayer MnN as an example of a 2D nodal-loop half-metal, with fully spin-polarized nodal loops that are robust against SOC. A previous work by Xu and Zhu [20] has demonstrated that monolayer MnN enjoys good dynamic and thermal stability, and it has a rigid ferromagnetic ordering. Here, we show that the electronic band structure of monolayer MnN features two fully spin-polarized nodal loops near the Fermi level. The two loops are centered around the Γ point, protected by a mirror symmetry and, more importantly, robust against SOC. We construct an effective model to describe the low-energy electronic states around the nodal loops. Furthermore, we find that moderate uniaxial strain can transform the outer nodal loop into two nodal loops, both traversing the BZ. This corresponds to a transition in the loop-winding topology, characterized by a $\mathbb{Z}^2$ index. Our work reveals a promising material platform for exploring the fundamental physics of fully spin-polarized 2D nodal-loop fermions, which also holds great potential for nanoscale spintronics applications.

II. COMPUTATIONAL METHOD

Our first-principles calculations were based on the density functional theory (DFT), as implemented in the Vienna *ab initio* simulation package (VASP) [21,22]. The interaction between electrons and ions was modeled using the projector augmented wave method [23]. The generalized gradient approximation (GGA) parameterized by Perdew, Burke, and Ernzerhof (PBE) was adopted for the exchange-correlation functional [24]. To account for the important correlation effect associated with the Mn-$3d$ orbitals, we included the Hubbard U correction via the PBE $+ U$ method [25]. Several Hubbard U values were tested, which showed qualitatively similar results. Below, we shall present the results with the U value set as 5 eV. A vacuum space of 20 Å thickness was used to avoid artificial interactions between periodic images. The energy cutoff was set to be 520 eV for the plane-wave basis. The Monkhorst-Pack k mesh [26] with size $25 \times 25 \times 1$ was adopted for the BZ sampling. The lattice parameters and the ionic positions were fully optimized until the residual force on each atom was less than 0.005 eV/Å. The energy convergence criterion was set to be 10^{-6} eV.

III. STRUCTURE AND ELASTIC PROPERTY

The lattice structure for monolayer MnN is shown in Figs. 1(a) and 1(b). The material is completely flat with a single atomic layer such as graphene. It takes a 2D honeycomb lattice, with Mn and N occupying the A and B sites, respectively. The space group is $P\bar{6}m2$ and the point group is D_{3h}. The important symmetry here is the horizontal mirror $\mathcal{M}_z$, which will play an important role when discussing the
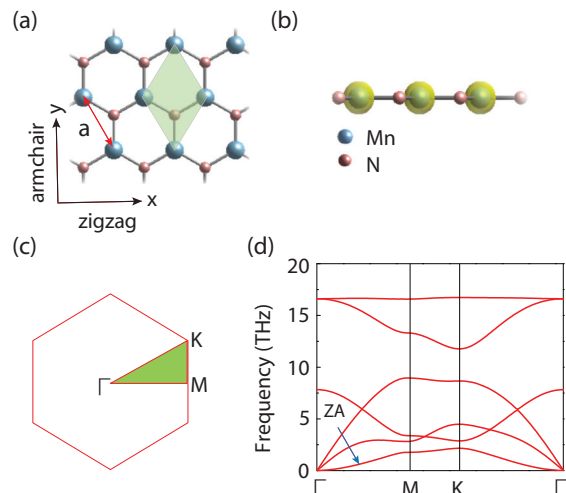

FIG. 1. (a) Top and (b) side view of the lattice structure for monolayer MnN. The green shaded region in (a) indicates the primitive unit cell. a is the lattice parameter. (b) The spin-polarization distribution. The yellow color indicates a net spin-up polarization. (c) Brillouin zone for monolayer MnN. (d) Calculated phonon spectrum. A 6×6 supercell is used in the calculation.

band structure. A primitive unit cell contains one Mn atom and one N atom. From our calculation, the equilibrium lattice constant is 3.388 Å for the fully relaxed structure, which is in good agreement with the previous work [20]. The obtained equilibrium Mn-N bond length is 1.956 Å.

The dynamical stability of monolayer MnN can be inferred from its phonon spectrum. As shown in Fig. 1(d), there is no imaginary-frequency phonon mode throughout the BZ, indicating that the material is dynamically stable. (We have also considered monolayer MnP and MnAs with the similar planar structure, but they are found to be unstable.) Approaching the Γ point, there are two linearly dispersing in-plane acoustic branches, and there is also a quadratic out-of-plane acoustic (ZA) branch. The appearance of the quadratic ZA branch is a characteristic feature of 2D materials [27–29]. The sound speed for the longitudinal acoustic phonons in monolayer MnN ($\sim$7.1 km/s) is smaller than that of graphene ($\sim$21.2 km/s) [30] as well as blue phosphorene ($\sim$8.1 km/s) [31], indicating that monolayer MnN should have relatively small in-plane stiffness, as we show below.

Next we examine the elastic properties. The calculated strain-stress and strain-energy curves are plotted in Fig. 2. One can observe that monolayer MnN can sustain a large biaxial strain up to 20%, while the critical uniaxial strain can be $\sim$18% for the armchair direction and $\sim$20% for the zigzag direction. These values are comparable to other 2D materials such as graphene [32], MoS_2 [33,34], phosphorene [35], and C_2N [36]. Monolayer MnN remains within the linear elastic regime until about 5% biaxial strain and 8% uniaxial strain. For small deformations, the elastic property of 2D materials is usually characterized by the in-plane stiffness constant, defined as

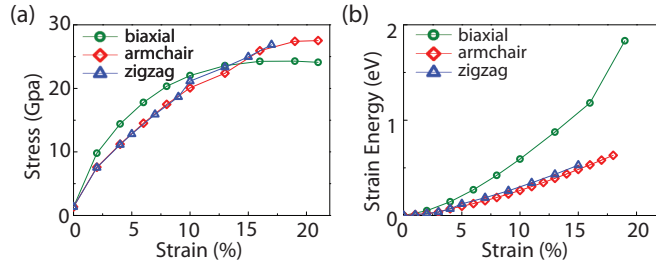$$C = \frac{1}{S_0} \frac{\partial^2 E_s}{\partial \varepsilon^2}, \tag{1}$$

FIG. 2. (a) Strain-stress relation for monolayer MnN with different types of strain. (b) Strain energy (E_s) as a function of applied strain.

where S_0 is the equilibrium area of the unit cell, E_s is the strain energy (i.e., the energy difference between the strained and unstrained systems), and ε is the in-plane uniaxial strain. From the stain-energy curve in Fig. 2(b), the typical quadratic dependence can be observed at small deformations. The obtained stiffness constants are 65 and 62 N/m for strains along the armchair and the zigzag directions, respectively. These values are smaller than other typical 2D materials such as graphene ($\sim 340 \pm 40$ N/m) [32], MoS_2 (~ 120 N/m) [37], and BN (~ 267 N/m) [38], and are similar to C_2N (~ 71 N/m) [36] and Mg_2C (~ 60 N/m) [39]. This indicates that monolayer MnN is quite flexible, which will facilitate the strain engineering of its physical properties.

IV. MAGNETIC PROPERTY

The $3d$ transition-metal elements such as Mn often carry magnetic moments due to their partially filled $3d$ shell. The materials containing Mn hence often exhibit magnetic ordering, which is the case for monolayer MnN. In our calculation, we compare the energies of different magnetic configurations: nonmagnetic (NM), ferromagnetic (FM), and antiferromagnetic (AFM), to determine the ground state of monolayer MnN. It is found that the FM state is energetically favored, while the NM sate and the AFM state are, respectively, 4.68 and 0.39 eV higher than the FM state per unit cell. In the FM state, the magnetic moment is mainly distributed on the Mn sites [see Fig. 1(b)], with $\sim 3.99\,\mu_B$ per Mn atom.

To pin down the easy axis for the FM state, the magnetic anisotropy energy calculation was performed by scanning different orientations for the magnetic moment with SOC included. The result shows that the out-of-plane (along z) configuration is most energetically favorable, which is about 0.4 meV lower in energy than the in-plane configuration. Thus, the ground-state magnetic configuration for monolayer MnN is an FM state with magnetization along the out-of-plane z direction.

We have also estimated the Curie temperature T_C for the FM state, by using the Monte Carlo simulation based on a classical Heisenberg-like spin model [40],

$$H = -J \sum_{\langle i,j \rangle} \mathbf{S}^i \cdot \mathbf{S}^j - K \sum_i \left(S_z^i \right)^2, \qquad (2)$$

where the spin vectors are normalized, the superscripts i and j label the Mn sites, $\langle i,j \rangle$ indicates nearest-neighboring sites, J is the FM exchange coupling strength, and K represents
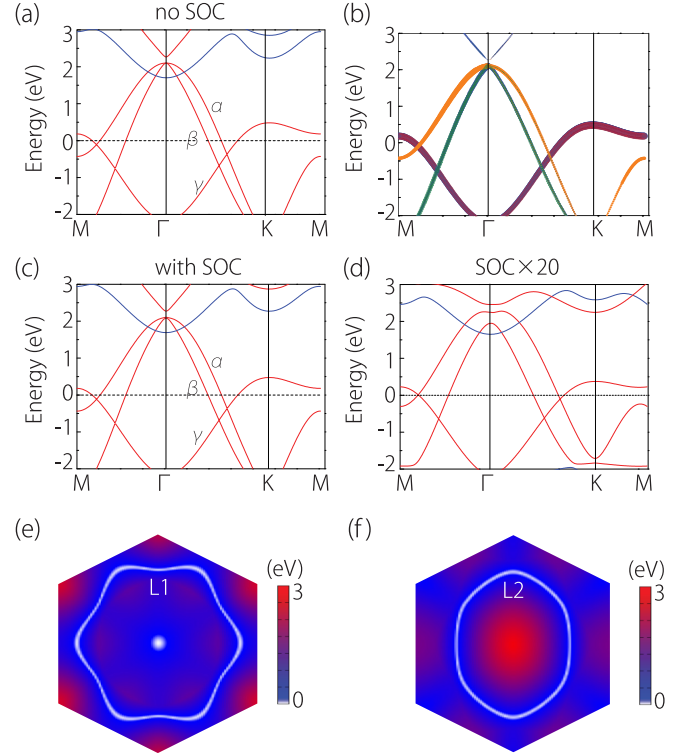

FIG. 3. (a) Calculated electronic band structure for monolayer MnN in the absence of SOC. (b) The projection of the bands in (a) onto atomic orbitals, including N p_x/p_y orbital (blue), N p_z orbital (red), Mn d_{xy} orbital (yellow), and Mn $d_{x^2-y^2}$ orbital (green). (c) Calculated band structure with SOC. (d) Band structure with SOC artificially enhanced by 20 times in the calculation. (e),(f) The shapes of the two nodal loops obtained by DFT calculation. The color map indicates the local gap between two crossing bands. In (a), (c), and (d), the red and blue colors indicate bands with fully polarized spin-up and spin-down states, respectively, showing that the two loops are fully spin polarized.

the magnetic anisotropy strength. The values of J and K extracted from DFT calculations are 0.25 and 0.412 meV, respectively. The calculated Curie temperature for monolayer MnN is around 200 K, which is comparable with other 2D ferromagnetic materials discovered to date, such as $Cr_2Ge_2Te_6$ atomic layers (~ 66 K) [41], transition-metal halides (23–128 K) [42,43], and Fe_3GeTe_2 (~ 130 K) [44].

V. 2D NODAL-LOOP HALF-METAL

The most interesting property of monolayer MnN lies in its electronic band structure. Let us first examine the band structure in the absence of SOC, as shown in Fig. 3(a). Two salient features can be observed. First, the ground state of monolayer MnN is a half-metal. The bands for majority spin (denoted as spin up) display a metallic behavior, whereas the bands for minority spin (denoted as spin down) have a large energy gap about 4.5 eV. The low-energy electrons near the Fermi level are therefore fully spin polarized. Second, several linear band crossings are observed for the majority spin bands close to the Fermi level. Among these low-energy bands, one is electronlike (labeled as γ band) and the other two are

holelike (labeled as α and β bands). From orbital projections in Fig. 3(b), we find that the α and β bands are mainly contributed by the Mn (d_{xy}, $d_{x^2-y^2}$) orbitals, while the γ band is mainly from the N p_z orbital. The band crossings occur between the γ band and the other two bands. A careful scan of the band structure shows that these crossing points are not isolated; instead, they actually belong to two concentric nodal loops centered around the Γ point, as shown in Figs. 3(e) and 3(f). We label the outer loop and the inner loop as L_1 and L_2, respectively.

Remarkably, the two nodal loops persist when SOC is turned on. Figure 3(c) shows the band structure with SOC included. The result is similar to that in Fig. 3(a). To show that the nodal loops are indeed preserved under SOC, we artificially increase the SOC strength by 20 times in the DFT calculation, and plot the resulting band structure in Fig. 3(d). It clearly shows that the crossings are robust against SOC. What protects the nodal loops? By analyzing the symmetry properties of the three bands, we find that the two loops are protected by the mirror symmetry $\mathcal{M}_z$. Because the ground-state magnetization is along the out-of-plane z direction, $\mathcal{M}_z$ is preserved in the FM state. The two holelike bands α and β have the $\mathcal{M}_z$ eigenvalue $+i$, whereas the electronlike band γ has the opposite $\mathcal{M}_z$ eigenvalue $-i$. Therefore, γ band must cross α and β bands without hybridization, and the resulting two loops are protected as long as the mirror symmetry is maintained. Furthermore, because of the $\mathcal{M}_z$ symmetry, the eigenstates must be spin polarized along z, i.e., the spin-up and spin-down bands do not hybridize and each band remains fully spin polarized. Thus, monolayer MnN indeed provides a 2D nodal-loop half-metal with fully spin-polarized nodal loops that are robust under SOC.

A nodal loop can be classified as type I, type II [45], or hybrid type [45,46], based on the type of dispersion around the loop. A type-I (type-II) nodal loop consists solely of type-I (type-II) nodal points, while a hybrid loop consists of both types [45,46]. The two nodal loops in monolayer MnN belong to type I because each is formed by the crossing between an electronlike band and a holelike band.

To characterize the emergent nodal-loop fermions, we construct an effective $k \cdot p$ model for the low-energy band structure. We choose the three states at the Γ point as the basis. We first consider the case without SOC. The state of the α band corresponds to the A_2'' irreducible representation for the D_{3h} point group, while the two degenerate states of β and γ bands correspond to the E' representation. The model should respect the following symmetries: the threefold rotation C_{3z}, the twofold rotation C_{2y}, and $\mathcal{M}_z$. Expanding up to the k quadratic order, we find that the effective Hamiltonian takes the form of

$$\mathcal{H}_0(\boldsymbol{k}) = \begin{bmatrix} M_0 + Ak_x^2 + Bk_y^2 & (B-A)k_xk_y & 0 \\ (B-A)k_xk_y & M_0 + Bk_x^2 + Ak_y^2 & 0 \\ 0 & 0 & M_1 + Ck^2 \end{bmatrix},$$
(3)

where M_i, A, B, and C are real-valued parameters which can be obtained from fitting the DFT band structure. Note that the matrix element between the α (β) and γ bands vanishes identically because the two bands have opposite $\mathcal{M}_z$ eigenvalues. Including SOC gives additional contribution, which can
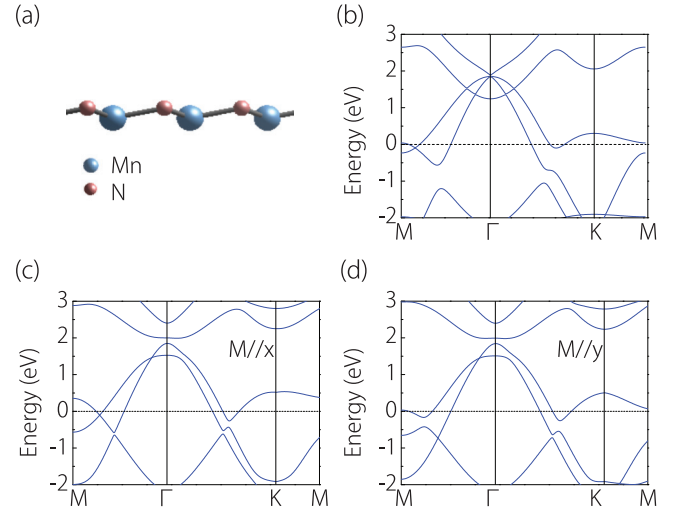

FIG. 4. (a) A lattice distortion that breaks the horizontal mirror reflection symmetry. Here, the monolayer shows a buckling with the Mn atoms shifted up relative to the N atoms. (b) Calculated band structure (including SOC) for the distorted structure in (a) when the shift is 0.2 Å. (c),(d) The band structures (including SOC) for an *undistorted* lattice, but with magnetic moments oriented in-plane along x and y directions, respectively.

be treated as a perturbation due to the relatively weak SOC strength. We find that the SOC term expanded to leading order takes the following form:

$$\mathcal{H}_{\text{SOC}}(\boldsymbol{k}) = \begin{bmatrix} 0 & iD & 0 \\ -iD & 0 & 0 \\ 0 & 0 & 0 \end{bmatrix},$$
(4)

with some real valued parameter D. Obviously, the SOC term does not affect the presence of the two nodal loops. Its main effect is that the degeneracy for the E' states is lifted. This effective model fits the DFT band structure very well (see the Supplemental Material [47]).

Breaking the mirror $\mathcal{M}_z$ would generally destroy the nodal loops. This can be done, e.g., by artificially shifting the Mn atoms along z relative to the N atoms, making a buckled honeycomb lattice [see Fig. 4(a)], or by orienting the magnetization direction in-plane. The corresponding band structure results in Figs. 4(b)–4(d) show that the two loops are indeed gapped out when $\mathcal{M}_z$ is broken.

VI. STRAIN-INDUCED NODAL-LOOP TRANSFORMATION

As discussed before, monolayer MnN enjoys good flexibility, hence its physical property should be readily tunable by strain. Here, we focus on the strain effect on the nodal loops. Since the two loops are protected by the horizontal mirror, they must be preserved under a variety of in-plane strains, such as the biaxial, uniaxial, and shear strains. Nevertheless, the shape of the loop may be changed by strain. For example, we consider the uniaxial strain along the armchair direction. Our result in Fig. 2(a) has shown that the critical strain is above 18%. In Fig. 5(a), we show the band structure result for
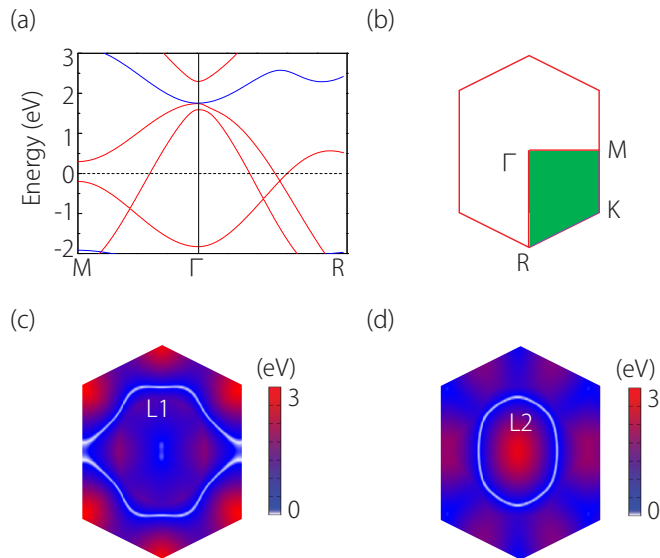
FIG. 5. (a) Calculated band structure for monolayer MnN with 7% uniaxial strain along the armchair direction. The red and blue colors represent spin-up and spin-down bands, respectively. (b) The corresponding Brillouin zone. (c),(d) The shapes of the corresponding nodal loops obtained from DFT calculation. L_1 is transformed into two extended loops traversing the Brillouin zone. The color map indicates the local gap between two crossing bands.

the 7% strain. One observes that while the loop L_2 remains a closed circle around the Γ point, the crossing point on Γ-M for loop L_1 disappears because the ordering between the α and γ bands at M is switched. Accordingly, the L_1 loop is transformed from a localized loop circling around Γ into two extended loops traversing the BZ, as shown in Fig. 5(c).

This transformation corresponds to a change in the loop-winding topology defined on the BZ. In Ref. [45], it has been shown that loops can be characterized by its winding pattern in the BZ, captured by the fundamental homotopy group for the BZ. For 2D, the BZ is a two-torus. Since $\pi_1(\mathbb{T}^2) = \mathbb{Z} \times \mathbb{Z}$, the topology is characterized by two integers, each standing for the number of times the loop winds around the BZ in a particular direction. For the current case, the original L_1 without strain is characterized by an index $(0,0)$, whereas the two loops after transformation [in Fig. 5(c)] are characterized by $(0, \pm 1)$. Their topological distinction can be understood in the following way. The loop with index $(0,0)$ can be continuously deformed into a point and annihilate, whereas a single loop with index $(0,1)$ cannot. Similar transformation was recently reported in the 2D honeycomb borophene oxide [9]. The monolayer MnN offers another platform for studying such interesting nodal-loop transformation.

VII. DISCUSSION AND CONCLUSION

We have a few remarks before closing. First, the finding reported here is significant because it reveals an example of a 2D nodal-loop half-metal and the loops are robust against SOC. Almost all the nodal loops in 2D reported so far are not robust under SOC. A nodal loop that is robust under SOC in 2D was noted by Young and Kane in a model study [14], and was recently found in the monolayer GaTeI family

materials [10]. However, these systems are nonmagnetic. It is very fortunate that the nodal loop, its robustness against SOC, and half metallicity can occur in the same material. Besides, the material band structure has the following two additional advantages: (i) The low-energy bands for monolayer MnN are fairly simple and clean, without other extraneous bands; and (ii) the linear dispersion range is also quite large (>1 eV).

Second, as the nodal loops here are protected by symmetry, their existence is not sensitive to the first-principles calculation methods. For example, we have verified that qualitative features of the band structure remain the same when using the hybrid functional (HSE06) approach. The result can be found in the Supplemental Material [47].

Third, when monolayer MnN is placed on a substrate, the interaction with the substrate would break the exact mirror symmetry and may open a gap at the nodal loop. Therefore, to study the nodal loop, it requires that the coupling with substrate must be weak. In practice, this has been achieved for many 2D materials grown on substrate. For example, it has been experimentally demonstrated that for Cu_2Si grown on Cu(111), the mirror symmetry breaking due to substrate has a negligible effect on the nodal loop because of the weak coupling between the 2D material and the substrate [11]. And this can be achieved by choosing a proper substrate and by a proper substrate surface treatment. In addition, we have also estimated the capability of monolayer MnN to form a freestanding membrane. Following the approach in Ref. [48], we find that even for large flakes with a size of 10^4 μm^2, the ratio between the out-of-plane deformation and the dimension of the monolayer is as small as 10^{-4}. This suggests that monolayer MnN is strong enough to form a freestanding membrane without substrate support. As such, we can get rid of the interaction from substrate, e.g., by placing the monolayer on a trench.

Finally, we remark on several other experimental aspects. It has been suggested that monolayer MnN can be synthesized by a spontaneous graphitic conversion from the ultrathin (111)-oriented cubic MnN in experiment [49]. The bottom-up approaches such as the molecular beam epitaxy (MBE) may also offer an alternative. It has been demonstrated that 2D monolayer CuSe with similar structure can be synthesized via the MBE approach with methane on the Cu(111) substrate [50]. The method is shown to be very versatile and can be used as a general strategy for fabricating other 2D materials. The nodal loops can be directly imaged by using the angle-resolved photoemission spectroscopy (ARPES), as recently demonstrated for monolayer Cu_2Si and CuSe [11,12]. The nodal loops may also produce features in the quasiparticle interference pattern which can be probed by the scanning tunneling microscopy experiment [51,52]. Techniques for applying strain on 2D materials have been well developed in recent years. For example, strain can be applied by using a beam-bending apparatus [53] or by using an atomic-force microscope tip [32]. By using a stretchable substrate, controllable strains >10% have been demonstrated for graphene [54].

In conclusion, we have revealed monolayer MnN as a 2D nodal-loop half-metal. We show that the material has good stability, can sustain large strains, and has excellent flexibility. The material has a FM ground state with an estimated

Curie temperature about 200 K. Most interestingly, its band structure shows a half-metal and features two concentric nodal loops near the Fermi level in a single spin channel. These nodal loops are protected by the mirror symmetry and are robust against SOC. We construct an effective model to characterize the emergent nodal-loop fermions. In addition, we find that a moderate uniaxial strain can generate an interesting loop topology transformation, from a single loop circling around Γ to two loops traversing the BZ. Our work thus provides a promising platform to investigate the intriguing properties of nodal-loop fermions with time-reversal breaking. We hope that our theoretical work will facilitate the experimental studies on this 2D material towards both fundamental discoveries and potential spintronics applications.

[1] K. S. Novoselov, A. K. Geim, S. V. Morozov, D. Jiang, Y. Zhang, S. V. Dubonos, I. V. Grigorieva, and A. A. Firsov, Science **306**, 666 (2004).

[2] S. Z. Butler, S. M. Hollen, L. Cao, Y. Cui, J. A. Gupta, H. R. Gutiérrez, T. F. Heinz, S. S. Hong, J. Huang, A. F. Ismach *et al.*, ACS Nano **7**, 2898 (2013).

[3] G. R. Bhimanapati, Z. Lin, V. Meunier, Y. Jung, J. Cha, S. Das, D. Xiao, Y. Son, M. S. Strano, V. R. Cooper *et al.*, ACS Nano **9**, 11509 (2015).

[4] K. S. Novoselov, A. Mishchenko, A. Carvalho, and A. H. Castro Neto, Science **353**, aac9439 (2016).

[5] A. H. Castro Neto, F. Guinea, N. M. R. Peres, K. S. Novoselov, and A. K. Geim, Rev. Mod. Phys. **81**, 109 (2009).

[6] Y.-J. Jin, R. Wang, J.-Z. Zhao, Y.-P. Du, C.-D. Zheng, L.-Y. Gan, J.-F. Liu, H. Xu, and S. Y. Tong, Nanoscale **9**, 13112 (2017).

[7] S. Li, Y. Liu, S.-S. Wang, Z.-M. Yu, S. Guan, X.-L. Sheng, Y. Yao, and S. A. Yang, Phys. Rev. B **97**, 045131 (2018).

[8] P. Zhou, Z. Ma, and L. Sun, J. Mater. Chem. C **6**, 1206 (2018).

[9] C. Zhong, W. Wu, J. He, G. Ding, Y. Liu, D. Li, S. A. Yang, and G. Zhang, Nanoscale **11**, 2468 (2019).

[10] W. Wu, Y. Jiao, S. Li, X.-L. Sheng, Z.-M. Yu, and S. A. Yang, Phys. Rev. Mater. **3**, 054203 (2019).

[11] B. Feng, B. Fu, S. Kasamatsu, S. Ito, P. Cheng, C.-C. Liu, Y. Feng, S. Wu, S. K. Mahatha, P. Sheverdyaeva *et al.*, Nat. Commun. **8**, 1007 (2017).

[12] L. Gao, J.-T. Sun, J.-C. Lu, H. Li, K. Qian, S. Zhang, Y.-Y. Zhang, T. Qian, H. Ding, X. Lin *et al.*, Adv. Mater. **30**, 1707055 (2018).

[13] C. L. Kane and E. J. Mele, Phys. Rev. Lett. **95**, 226801 (2005).

[14] S. M. Young and C. L. Kane, Phys. Rev. Lett. **115**, 126803 (2015).

[15] S. Guan, Y. Liu, Z.-M. Yu, S.-S. Wang, Y. Yao, and S. A. Yang, Phys. Rev. Mater. **1**, 054003 (2017).

[16] C. Niu, P. M. Buh, H. Zhang, G. Bihlmayer, D. Wortmann, S. Blügel, and Y. Mokrousov, arXiv:1703.05540.

[17] B. Wang, H. Gao, Q. Lu, W. H. Xie, Y. Ge, Y.-H. Zhao, K. Zhang, and Y. Liu, Phys. Rev. B **98**, 115164 (2018).

[18] B. Feng, R.-W. Zhang, Y. Feng, B. Fu, S. Wu, K. Miyamoto, S. He, L. Chen, K. Wu, K. Shimada *et al.*, arXiv:1901.01429.

[19] C. Chen, Z.-M. Yu, S. Li, Z. Chen, X.-L. Sheng, and S. A. Yang, Phys. Rev. B **99**, 075131 (2019).

[20] Z. Xu and H. Zhu, J. Phys. Chem. C **122**, 14918 (2018).

[21] G. Kresse and J. Hafner, Phys. Rev. B **47**, 558 (1993).

[22] G. Kresse and J. Furthmüller, Phys. Rev. B **54**, 11169 (1996).

[23] P. E. Blöchl, Phys. Rev. B **50**, 17953 (1994).

[24] J. P. Perdew, K. Burke, and M. Ernzerhof, Phys. Rev. Lett. **77**, 3865 (1996).

[25] S. L. Dudarev, G. A. Botton, S. Y. Savrasov, C. J. Humphreys, and A. P. Sutton, Phys. Rev. B **57**, 1505 (1998).

[26] H. J. Monkhorst and J. D. Pack, Phys. Rev. B **13**, 5188 (1976).

[27] H. Zabel, J. Phys. Condens. Matter. **13**, 7679 (2001).

[28] L. Zhu, G. Zhang, and B. Li, Phys. Rev. B **90**, 214302 (2014).

[29] J. Carrete, W. Li, L. Lindsay, D. A. Broido, L. J. Gallego, and N. Mingo, Mater. Res. Lett. **4**, 204 (2016).

[30] K. Kaasbjerg, K. S. Thygesen, and K. W. Jacobsen, Phys. Rev. B **85**, 165440 (2012).

[31] Z. Zhu and D. Tománek, Phys. Rev. Lett. **112**, 176802 (2014).

[32] C. Lee, X. Wei, J. W. Kysar, and J. Hone, Science **321**, 385 (2008).

[33] A. Castellanos-Gomez, M. Poot, G. A. Steele, H. S. Van der Zant, N. Agraït, and G. Rubio-Bollinger, Nanoscale Res. Lett. **7**, 233 (2012).

[34] S. Bertolazzi, J. Brivio, and A. Kis, ACS Nano **5**, 9703 (2011).

[35] X. Peng, Q. Wei, and A. Copple, Phys. Rev. B **90**, 085402 (2014).

[36] S. Guan, Y. Cheng, C. Liu, J. Han, Y. Lu, S. A. Yang, and Y. Yao, Appl. Phys. Lett. **107**, 231904 (2015).

[37] Q. Peng and S. De, Phys. Chem. Chem. Phys. **15**, 19427 (2013).

[38] M. Topsakal, S. Cahangirov, and S. Ciraci, Appl. Phys. Lett. **96**, 091912 (2010).

[39] S.-S. Wang, Y. Liu, Z.-M. Yu, X.-L. Sheng, L. Zhu, S. Guan, and S. A. Yang, Phys. Rev. Mater. **2**, 104003 (2018).

[40] R. F. Evans, W. J. Fan, P. Chureemart, T. A. Ostler, M. O. Ellis, and R. W. Chantrell, J. Phys. Condens. Matter. **26**, 103202 (2014).

[41] C. Gong, L. Li, Z. Li, H. Ji, A. Stern, Y. Xia, T. Cao, W. Bao, C. Wang, Y. Wang *et al.*, Nature (London) **546**, 265 (2017).

[42] B. Huang, G. Clark, E. Navarro-Moratalla, D. R. Klein, R. Cheng, K. L. Seyler, D. Zhong, E. Schmidgall, M. A. McGuire, D. H. Cobden *et al.*, Nature (London) **546**, 270 (2017).

[43] V. V. Kulish and W. Huang, J. Mater. Chem. C **5**, 8734 (2017).

[44] Z. Fei, B. Huang, P. Malinowski, W. Wang, T. Song, J. Sanchez, W. Yao, D. Xiao, X. Zhu, A. F. May *et al.*, Nat. Mater. **17**, 778 (2018).

[45] S. Li, Z.-M. Yu, Y. Liu, S. Guan, S.-S. Wang, X. Zhang, Y. Yao, and S. A. Yang, Phys. Rev. B **96**, 081106(R) (2017).

[46] X. Zhang, Z.-M. Yu, Y. Lu, X.-L. Sheng, H. Y. Yang, and S. A. Yang, Phys. Rev. B **97**, 125143 (2018).

[47] See Supplemental Material at http://link.aps.org/supplemental/10.1103/PhysRevMaterials.3.084201 for the result obtained by the hybrid functional approach and model fitting of the DFT band structure.

[48] T. J. Booth, P. Blake, R. R. Nair, D. Jiang, E. W. Hill, U. Bangert, A. Bleloch, M. Gass, K. S. Novoselov, M. I. Katsnelson *et al.*, Nano Lett. **8**, 2442 (2008).

[49] P. B. Sorokin, A. G. Kvashnin, Z. Zhu, and D. Tomanek, Nano Lett. **14**, 7126 (2014).

[50] X. Lin, J. Lu, Y. Shao, Y. Zhang, X. Wu, J. Pan, L. Gao, S. Zhu, K. Qian, Y. Zhang *et al.*, Nat. Mater. **16**, 717 (2017).

[51] H. Zheng, S.-Y. Xu, G. Bian, C. Guo, G. Chang, D. S. Sanchez, I. Belopolski, C.-C. Lee, S.-M. Huang, X. Zhang *et al.*, ACS Nano **10**, 1378 (2016).

[52] Z. Zhu, T.-R. Chang, C.-Y. Huang, H. Pan, X.-A. Nie, X.-Z. Wang, Z.-T. Jin, S.-Y. Xu, S.-M. Huang, D.-D. Guan *et al.*, Nat. Commun. **9**, 4153 (2018).

[53] H. J. Conley, B. Wang, J. I. Ziegler, R. F. Haglund, Jr., S. T. Pantelides, and K. I. Bolotin, Nano Lett. **13**, 3626 (2013).

[54] K. S. Kim, Y. Zhao, H. Jang, S. Y. Lee, J. M. Kim, K. S. Kim, J.-H. Ahn, P. Kim, J.-Y. Choi, and B. H. Hong, Nature (London) **457**, 706 (2009).